STARS

University of Central Florida
STARS

Faculty Bibliography 1990s

Faculty Bibliography

1-1-1996

Scanning Heterodyne Optical Interferometers

Nabeel A. Riza
University of Central Florida

Find similar works at: https://stars.library.ucf.edu/facultybib1990

University of Central Florida Libraries http://library.ucf.edu

Recommended Citation

Riza, Nabeel A., "Scanning Heterodyne Optical Interferometers" (1996). *Faculty Bibliography 1990s*. 1739.
https://stars.library.ucf.edu/facultybib1990/1739

Showcase of Text, Archives, Research & Scholarship

Nabeel A. Riza

View Online   Export Citation

ARTICLES YOU MAY BE INTERESTED IN
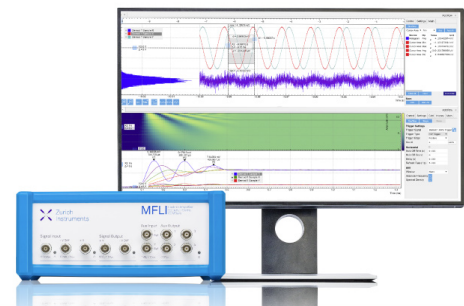
Scanning heterodyne optical interferometers

Nabeel A. Riza[a)]

Center for Research & Education in Optics and Lasers (CREOL), Department of Electrical and Computer Engineering, University of Central Florida, P.O. Box 162700, Orlando, Florida 32816-2700

Compact, high performance, scanning heterodyne optical interferometers are introduced for interferometric phase-based measurement applications. The novel, in-line, almost common-path optical interferometer design offers robustness to externally induced phase noise via mechanical vibrations, thermal effects, and other environmental effects. Novel instrument designs are introduced for both transmissive and reflective interferometry. These instruments use acousto-optic devices or Bragg cells to implement rapid (e.g., <50 μs/scan spot) optical scanning of the test medium. Although the read optical beam scans a given test region, the double Bragg diffraction optical design of the instrument makes the final interfering output beams stationary on the two high speed photodetectors used for radio frequency signal generation via heterodyne detection. One photodetector acts as the fixed phase reference, while the other fixed photodetector picks up the test medium phase information as the optical beam scans the test region. The transmissive design instrument is built in the laboratory using flint glass Bragg cells. A typical 120 MHz heterodyne detected signal output had a carrier-to-noise ratio of 108.9 dBc/Hz measured at a $+160$ kHz offset using a spectrum analyzer resolution bandwidth of 30 kHz. The corresponding single-sideband phase noise was estimated at -101.57 dBc/Hz at 160 kHz offset. The measured instrument radio frequency dynamic range was $\sim$60 dB or an equivalent of 30 dB optical dynamic range, with a 1/1000 of a fringe cycle phase measurement accuracy. Test medium optical phase mapping was successfully tested with the instrument using a large area, 6 μm thick, birefringent-mode nematic liquid crystal cell. Our instrument allows the use of high continuous wave or peak power, broad spectral linewidth, coherent light sources. The instrument can have a high 50% optical power efficiency. High speed two-dimensional optical scanning of a test medium is possible with our instrument by using a fixed one-dimensional output high speed detector array, or via the use of high speed nonmechanical electro-optic deflectors. © *1996 American Institute of Physics.* [S0034-6748(96)01507-9]

I. INTRODUCTION

It is well known that optical interferometry plays a vital and useful role in scientific and industrial applications. Over the years, optical interferometry has been used for a wide variety of applications that include measurements of material thickness and changes in thickness, surface structure characterization, gas flow, and plasma temperature measurement, particle velocity measurement, electric and magnetic field sensing, rotation and stress measurements, and a host of other applications.[1,2] Depending on the application requirements, one optical interferometer might be preferred over the other. One basic phase measurement method, the quasihetrodyne phase-step method, is where the local intensity of the interference pattern is sampled at fixed phase steps.[3] This method allows only modulo-2π interference measurements; and to get a complete phase map, the continuity of the phase function is assumed, and well known phase interpolation techniques are used.[4] This method typically offers a 1/100 of a fringe interference phase measurement accuracy. An interferometer that offers higher accuracy, i.e., better than 1/1000 of a fringe, interference phase measurement and also does away with both the phase interpolation problem (in quasihet-

erodyne methods) and the sign ambiguity of classical interferometry, is the heterodyne interferometer.[3,5,6] In this interferometer, a high speed photodetector generates an electrical signal via heterodyne detection of the interfering signal and reference optical beams that have slightly different (e.g., by 1 MHz) optical frequencies. The phase of this heterodyne detected electrical signal relative to an external stable electrical signal determines the measured local optical phase of the test medium. An electronic phase-meter is typically used to measure the phase between the two electrical signals.[7] Using this localized phase information and mechanically scanning the test medium by motion of a detector, the overall phase distribution of the test medium can be reconstructed for test and evaluation purposes.

One such use of the heterodyne interference method was implemented for strain measurements via a two reference beam, holographic interferometric setup.[8,9] Here, a frequency difference of 100 kHz between the two reference beams during the reconstruction process was generated using two acousto-optic modulators (AOMs) set for opposite Doppler shifts, with one AOM driven by 40 MHz and the other by 40.1 MHz. The phase differences between the two 100 kHz beat signals generated at the output photo-detector pair are measured using a zero-crossing electronic phase-meter which interpolates the phase angle to 0.1° and also counts the mul-

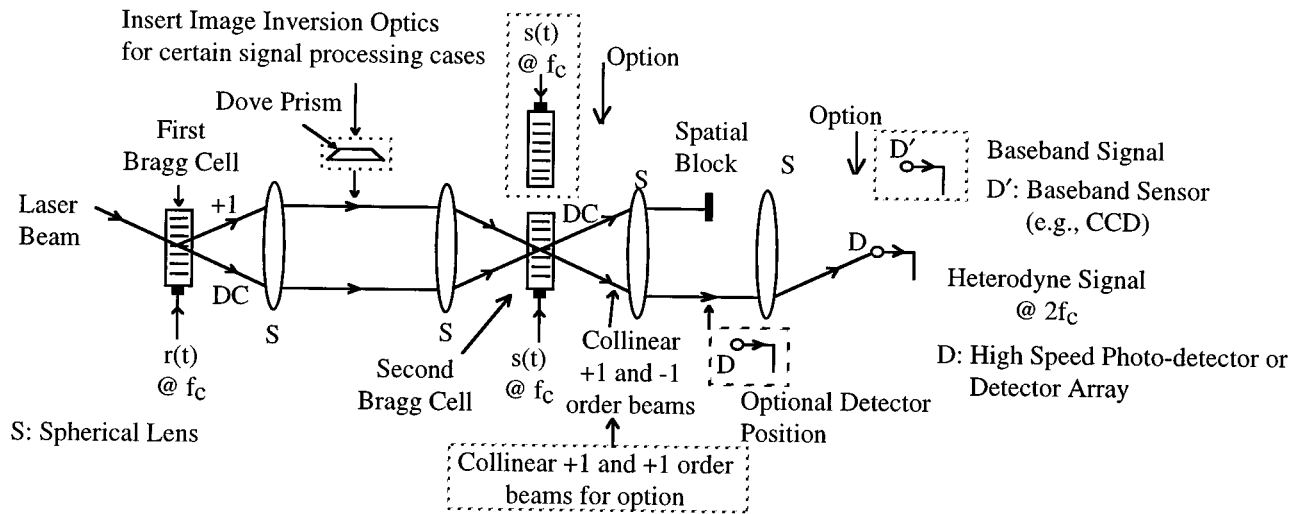[a)]Electronic mail: riza@creol.ucf.edu

FIG. 1. The basic in-line acousto-optic interferometer architecture developed by N. A. Riza for several photonic signal processing applications that include phased array antenna control, rf signal correlation, convolution, spectrum analysis, and notch filtering operations.

tiples of 360°. One important conclusion of this heterodyne experiment was that the heterodyne fringe interpolation technique did not restrict the phase measurement accuracy. In fact, it was mainly the air turbulence and mechanical hologram repositioning that limited instrument performance.

Another heterodyne interferometer measurement instrument was tested recently using phase-locked piezoelectric transducer (PZT)-tunable diode-pumped Nd YAG lasers and acousto-optic (AO) devices.[10] A common theme with nearly all heterodyne interferometers is the use of the Doppler shifting property of AO devices to generate the color shifts in the optical beams used in the interferometry. These AO device-based interferometers are constructed using several mirrors, beamsplitters, beam combiners, and possibly a host of other optical and mechanical components laid out over a large test area (e.g., 1 m^2). Furthermore, mechanical motion of mirrors is typically used for scanning the optical beams used in the interference process for gathering phase data for a given test area. Because each component of the interferometer is a possible source of unwanted phase noise (e.g., through mechanical vibration of a mirror), in general, these heterodyne optical interferometers have to be built on costly air-isolation optical tables with special thermal and mechanical vibration protection. With these two limitations in mind, i.e., mechanical beam scanning and vibration stability, in this article, we introduce a new kind of heterodyne optical interferometer that has high speed nonmechanical inertialess beam scanning capabilities, plus a compact in-line design for minimizing air turbulence and other unstable phase noise effects.

II. BASIC ACOUSTO-OPTIC IN-LINE INTERFEROMETER FOR PHOTONIC SIGNAL PROCESSING

Over the last several years, the author has developed and experimentally demonstrated a compact, heterodyne and baseband-type optical interferometer architecture for a host of photonic information processing applications such as phased array antenna/radar control[11–15] and radio frequency

(rf) signal correlation,[16] convolution,[17] notch filtering,[18] and spectrum analysis operations.[19] This interferometric architecture is shown in Fig. 1, and consists of two AO devices or Bragg cells in an in-line configuration, where the first Bragg cell acts as an optical beam splitter, and the second Bragg cell acts as an optical beam combiner. Thus, using only four optical components (two Bragg cells and two lenses)—all in the path of the interfering optical beams—one is able to realize a compact, low component count interferometer. This heterodyne/baseband interferometer has an important property that is desirable for all optical interferometers; namely, excellent mechanical stability and tolerance to optical phase instabilities via the almost common-path in-line design. Notice that the system is perfectly collinear, except between the two Bragg cells where the two interfering beams are physically separated, although, still in-line and in close proximity (e.g., 1 cm). Thus, any thermal, mechanical, or air turbulence effects impinging on this instrument are suffered almost exactly by both interfering beams on the photodetector. In fact, the heterodyne detection operation via optical mixing at the photodiode results in the cancellation of this phase noise. The following section gives a concise but instructional account of the inner workings of this interferometer, as this design is closely related to the novel scanning interferometers introduced in this article.

As shown in Fig. 1, light from an input laser is Bragg matched to the first Bragg cell that is fed by a rf signal centered at a frequency f_c. For low diffraction efficiencies (e.g., <10%) required for linear AO signal modulation, the first Bragg cell produces a strong undiffracted dc beam and a weaker, deflected, positive Doppler shifted, +1 order diffracted beam. Thus, this first Bragg cell creates the two beams required in this interferometer. 1:1 imaging optics are used to image the first Bragg cell plane onto the second Bragg cell plane. Note that the imaging preserves the Bragg matching condition at the second Bragg cell that is also fed by a rf signal centered at a frequency f_c. The strong dc beam from the first Bragg cell generates a weaker, deflected, nega-

tive (or positive) Doppler shifted, -1 (or $+1$) order diffracted beam from the second Bragg cell. Note that after the second Bragg cell, the $+1$ and -1 (or $+1$) order beams are collinear, implying that the second Bragg cell also acts as a beam combiner for the interferometer. Depending on the desired information processing application, the $+1$ and -1 order beams or the $+1$ and $+1$ order beams (shown as an option) are interfered and heterodyne detected by an appropriately positioned photodetector or arrays of detectors at the desired output plane. As shown in Fig. 1, the two-beam interference can be detected at either the Fourier plane of the second Bragg cell, or the image plane of the second Bragg cell. The beat rf signal generated by the interference sensing photodetector is centered at a $2f_c$ frequency carrier for the $+1$, -1 order case, and is modulated by the required signal processing transform output signal desired from the photonic processor. In the optional case, the $+1$, $+1$ orders interfere to generate the desired baseband output signal. Because a Bragg cell is an excellent device for introducing rf or wideband (e.g., 50 MHz to 1 GHz instantaneous bandwidth) electrical signals onto the Bragg diffracted optical beam, it thus becomes possible to use this interferometer to optically process a variety of electrical signals; in particular, the electromagnetic interference (EMI) sensitive microwave or higher band electrical signals. Thus, the author proposed and experimentally demonstrated several versions of this interferometer (see Fig. 1) as various significant coherent signal processors.[11–19]

As mentioned in the Introduction of this article, it would be extremely desirable to have an optical heterodyne interferometer that has good phase/mechanical stability, plus nonmechanical optical beam scanning capability for rapid inspection and evaluation of a test medium. In the rest of this article, we will show how a modification to the basic optical heterodyne (or baseband) interferometer in Fig. 1 will allow us to realize a novel high speed scanning optical interferometer with excellent mechanical stability and phase noise suppression characteristics.

III. PROPOSED SCANNING HETERODYNE OPTICAL INTERFEROMETER

A. Transmissive mode design: Theory and experiment

Figure 2 shows the novel scanning heterodyne optical interferometer for transmissive optical sensing applications that is also experimentally setup in the laboratory. The overall optical layout of our proposed interferometer is similar to the earlier developed AO interferometer shown in Fig. 1. This basic architectural and component similarity gives our proposed interferometer its exceptional mechanical/vibrational stability and component simplicity. There is also a critical design difference in which light beams generate the desired test medium phase information on the fixed (along the x-direction) heterodyne photodetectors at the output interference plane. Because we want to form a high speed nonmechanical scanning interferometer—where a particular beam scans the test medium while a fixed photodetector at the output interference plane picks up the required phase

information—we need to keep the final output plane collinear interfering beams fixed at this detector location. In our proposed design in Fig. 2, this is accomplished using Bragg diffractions of the signal (or test) beam at both Bragg cells in the system. Thus, the double diffraction process prevents the scanned beam from moving at the final output/detection plane, and a single fixed photodetector is sufficient to generate the desired phase-modulated $2f_n$ carrier signal. Nevertheless, the test beam (the diffracted order) between the two Bragg cells does indeed rapidly scan the test medium along the x direction as a stepped frequency linear frequency modulated (FM) signal is fed to both Bragg cells. Thus, the instrument performs the required high speed electronically controlled optical scanning of the test zone that is inserted in the instrument for phase/material feature mapping purposes.

To minimize redundancy, both the theory and the experiment for our proposed interferometer in Fig. 2 are explained together. Horizontally or p-polarized light from a 100 mW, 532 nm, diode-pumped Nd:YAG laser passes through a spatial filter assembly consisting of an objective lens ($\times 40$, NA $=0.65$) and a 15 μm diameter pinhole. A 5 cm focal length (FL) spherical lens S is used to collimate the laser light. Using a 30 cm FL cylindrical lens C1, the collimated laser light is Bragg-matched as a line in the first AO deflector (AOD1). AOD1 and AOD2 (the second Bragg cell in the system) are flint glass Bragg-cells from IntraAction Corp. with a center frequency of 70 MHz and a bandwidth of 40 MHz (at 633 nm). Both AODs have an operating wavelength of 400–700 nm with $\lambda=633$ nm being the design wavelength. The active AOD aperture is 39 mm$\times$2 mm and the access time is 10 μs. The maximum driving power for these devices is 4 W and the input impedance is 50 Ω. Both AOD1 and AOD2 are driven by a sinusoidal signal of frequency f_n from a sweep generator where f_n corresponds to the stepped frequency at the nth spatial point scanned by the optical beam on the test medium. n varies from 1,2,...,N, where N is an integer representing the maximum number of scanned positions along the x-direction on the test medium. In the experiment, both Bragg cells are driven by 0.73 W single tone rf signals (in the range from 50 to 90 MHz) from a Wavetek model 5135A frequency synthesizer. The Bragg matched diffraction efficiency for the $+1$ orders measured for this rf AOD drive power for both Bragg cells was 40%. Using the well-known Bragg diffraction condition, the deflection angle (relative to the undiffracted dc beam) for these flint glass Bragg cell devices with an acoustic signal velocity of $v_a=3.846$ mm/μs can be approximately given by

$$\theta_d(\text{mrad})=[\lambda(\mu m)\times f_n(\text{MHz})]/[v_a(\text{mm}/\mu s)]. \qquad (1)$$

This relation along with the FL F1 of the imaging lens S1 determines the limits to the test medium scan area of our proposed interferometer. Using this relation, the dc and $+1$ beam separation at the test medium plane can be approximately given by the design relation

$$\Delta x_{\text{dc},+1}=\theta_d\text{F1}, \qquad (2)$$

where F1 is the FL of the lens S1 after AOD1. These system issues along with scanning along the vertical or y-direction of the test medium will be discussed later in the article.
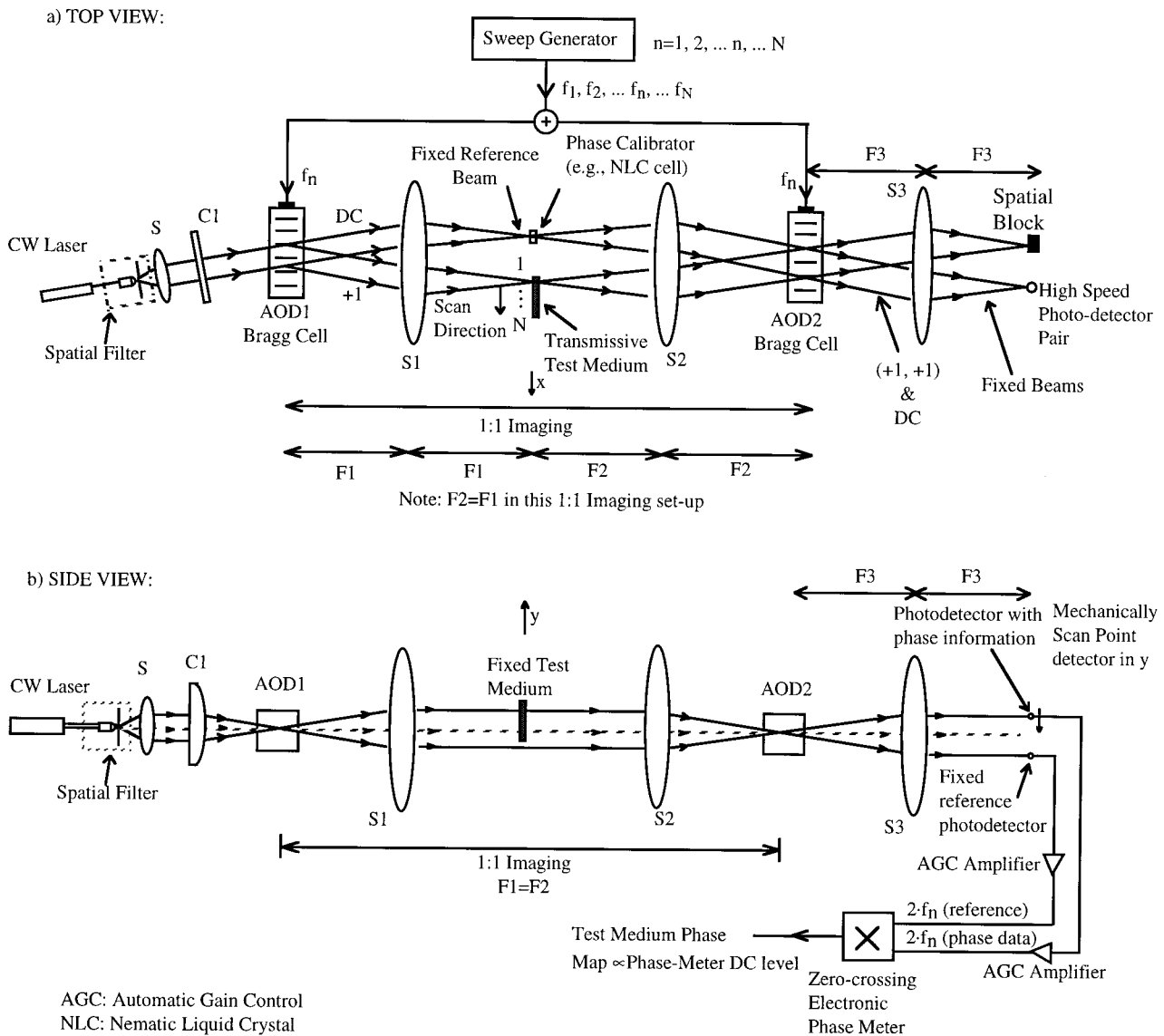
a) TOP VIEW:

FIG. 2. The novel scanning heterodyne optical interferometer for transmissive optical measurement and sensing applications.

The light output from AOD1 consists of a dc or undiffracted beam and a +1 positive Doppler shifted diffracted beam. These dc and +1 order beams are 1:1 imaged by a two lens imaging system onto AOD2. The two lenses S1 and S2 have FLs F1 and F2, respectively, with F1=F2=15 cm, as we need to form a 1:1 imaging system. The +1 diffracted order passes through the test medium and is then diffracted one more time by AOD2, while a large portion of the dc beam from AOD1 passes through AOD2. The +1 double diffracted beam produced by AOD1 and AOD2 Bragg diffractions, and the dc beam originally coming from the laser source, become collinear after AOD2. When the test medium is optically scanned in the x-direction by feeding the Bragg cells with a frequency swept signal, only the +1 double diffracted beam and dc beam from the laser stay fixed on the photodetector that is positioned at the Fourier plane of the second Bragg cell. The other diffracted beam pair from the Bragg cells does not remain stationary, and is, therefore, blocked at the output interference plane using a spatial block. A F3=12.5 cm FL lens S3 is used the separate the desired

and unwanted beam pairs in space to do the spatial filtering.

Notice from the side view of the system in Fig. 2 that a minimum of two spatially separate high speed detectors are required at the interference plane of the system. This is because the lower detector (along the y direction) generates the $2 f_n$ frequency phase-reference signal for the electronic phase meter (mixer), while the heterodyne detected $2 f_n$ frequency signal coming from the top fixed (along the x-scan direction) photo detector contains the test medium phase data. Note from Fig. 2 (side view) that the reference beams do not pass through the test medium. Both the reference-phase and test medium-phase $2 f_n$ frequency signals are fed to the electronic phase-meter for test medium phase map generation. Note that after dc electrical bias removal, the heterodyne signal generated by the top photodiode can be expressed as

$$i_s(t,n,m) = A_{nm} \cos[2\pi(2f_n)t - \theta_{nm}], \qquad (3)$$

while the reference-phase signal from the bottom photodiode can be expressed as

$$i_R(t) = A_{dnm} \cos[2\pi(2f_n)t], \qquad (4)$$

where A_{dnm} is a variable amplitude level generated mainly due to the nonuniform diffraction efficiency of the Bragg cells over the scan range, and A_{nm} is the mnth scan position dependent variable amplitude level that is determined mainly by the transmittance function of the test medium and the Bragg cell diffraction efficiencies. θ_{nm} is the optical phase suffered by the scan beam at the nth x-direction scan position and mth y-direction scan position of the test medium. Using automatic gain controlled (AGC) amplifiers on both the test scan signal chain and the reference signal chain, fixed amplitude level reference and test scan signals are fed to the phase meter. Constant amplitude signals must be fed to the phase meter to get accurate phase data readings as the phase meter operates as a signal mixer and low pass filter that generates a dc level that is proportional to the phase difference between the two signals. This technique has been used previously with high success with better than 0.1° phase measurement accuracy.[7,9]

Note that we have used the y-scan index m to represent test medium scanning in the vertical or y-direction. This y-direction scanning can be achieved in two ways using the system in Fig. 2. In one design, because a vertical line scans the test medium in the x-direction via the use of Bragg cells, a vertical line also appears at the output interference plane. Thus, by mechanically scanning the top detector in the y-direction after completing the N x-scan positions, a complete $x-y$ two-dimensional phase map of the test medium can be generated. The other approaches which do away with the point detector y motion is to replace the single top detector with a K-element linear high speed detector array in the y direction. In this way, the output of the system are K simultaneous $2f_n$ frequency phase modulated signals corresponding to the K resolution points along the y-direction on the test medium. This method does away with mechanical motion at the cost of introducing parallel phase-detection electronics. Another option is to use a pair of electro-optic (EO) y direction deflectors that are cascaded to the two AODs.[20] For instance, nematic liquid crystal (NLC) devices could be used to form one-dimensional optical beam deflectors.[21] Also, bulk crystal EO deflectors can be used for the y-direction beam deflection. These and other options will be described in future work related to these instruments.

In our experiment, we use two high speed photodetectors from New Focus, Inc. These Model 1801 high speed photoreceivers have 0.9 mm active diameters with detector operation from dc-120 MHz. Note that at the focal plane of lens S1 where the vertical line shape dc beam passes, we can place a programmable optical phase modulation device (or array of devices along the y direction) for phase error cancellation and system phase calibration purposes. For instance, possible phase errors in the external reference and scan signal chain electronics can be calibrated by setting the optical phases on this electronically controlled phase shifter array to the desired values for the spatially different (along the y-direction) dc reference beams corresponding to the different $+1$ order reference and scan signal beams along the y direction at the Fourier plane of S1. For instance, the reference-phase heterodyne detected signal from the bottom detector at the output plane can be calibrated to have the appropriate phase relative to the scan signals such that various component-based serial signal path phase errors are minimized, thus leading to accurate phase measurements via the electronic zero-crossing phase meter. One high grey-scale analog (e.g., >10 bits) option for this calibration optical phase shifter array is a parallel-rub birefringent-mode NLC device where the NLC device is placed with its nematic director parallel to the p-polarized incident light from the laser. By changing the applied 0–5 V, 1 kHz square wave signal used to drive the NLC device, the phase of the distributed reference or dc light beams can be controlled in our interferometer.

With no test material in the scan beam path between the two Bragg cells, and using a 10 times attenuation neutral density filter between AOD2 and sphere S3 to prevent photoreceiver saturation effects, rf powers of -38.52 and -32.5 dBm are generated by the scan beam photoreceiver and the reference beam photoreceiver, respectively, when using 60 MHz AOD drive signals. Note that because of the large physical size of the New Focus photoreceiver package, a cube beam splitter was placed after the sphere S3 to generate two output planes so that the two photoreceivers could be easily placed at the two different output planes. Thus, because of the splitting of the light energy, lower useful optical power is detected in this experiment. Note from the side view in Fig. 2 that the two photodiodes monitor the reference and scan signal beams. A modulation depth of approximately 90% is measured for both 120 MHz signals generated via heterodyne detection at the photoreceivers. Modulation depth$=(V_{max}-V_{min})/(V_{max}+V_{min})\times100\%$, where V_{max} and V_{min} are the maximum and minimum voltage levels, respectively, of the $2f_n$ frequency output signal. Because the zero Doppler shifted reference beam is somewhat stronger than the double diffracted $2f_n$ Doppler shifted scanned beam (recall that the Bragg cells were operated at near 40% diffraction efficiency (d.e.), not 50% d.e.), a slightly higher dc bias level signal is generated in the photodetected signals. Using ac-coupled IntraAction Corp. Model PA-4 power amplifiers with 40 dB gain, the dc bias levels are filtered out, and the ac signals are amplified for viewing and phase measurements using an oscilloscope and a spectrum analyzer.
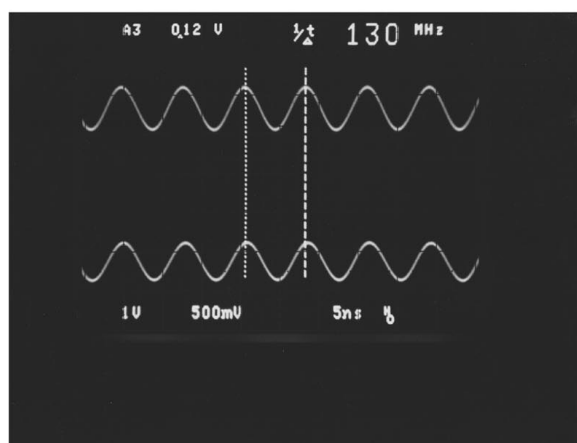
Figure 3 shows the oscilloscope traces of the amplified outputs from the reference and scan photoreceivers, when no test material is inserted into the system. Note that regardless of the value of the AOD drive frequency required for scanning the optical beam, the relative phase between the reference and scan photodetector output signals remains constant. In fact, with accurately matched rf cable lengths, and symmetrically positioned optical components, the relative time/phase delay between the two detected signals should be zero, as all optical and electrical path lengths are identical. In Fig. 3, we see essentially in-phase reference (top trace) and scan signals (bottom trace) for (a) 60 MHz and (b) 65 MHz AOD drive frequency conditions, generating 120 MHz and 130 MHz heterodyne detected signals, respectively. Thus, with no test material inserted in the laboratory instrument, the signal pair generated by the photodetector pair remained in-
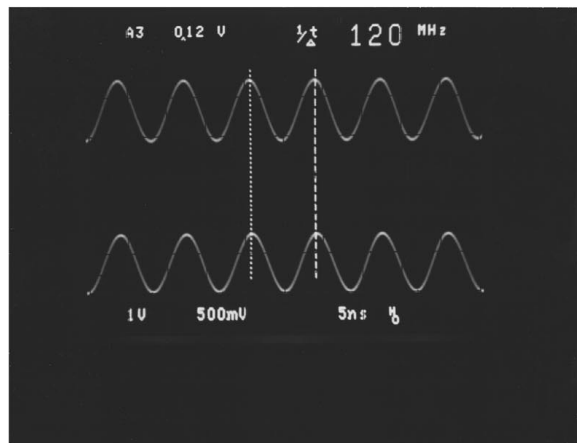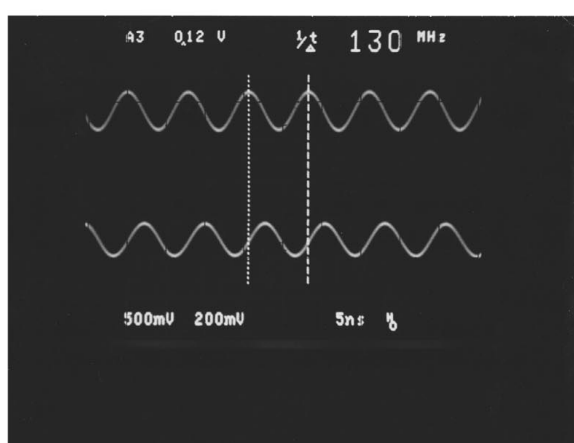
(a)
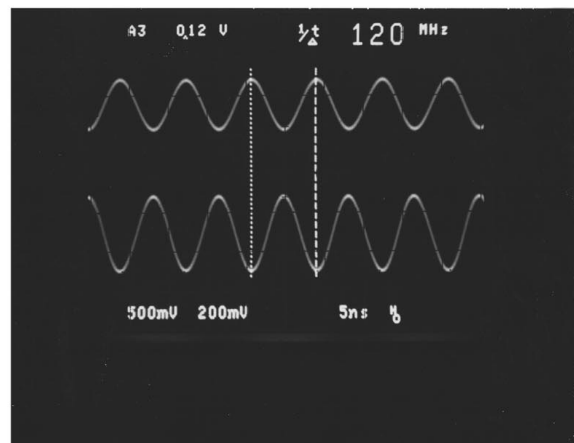
(a)

(b)

(b)

FIG. 3. Oscilloscope traces of the amplified outputs from the reference and scan photoreceivers, when no test material is inserted into the system. We see essentially in-phase reference (top trace) and scan signals (bottom trace) for (a) 60 MHz and (b) 65 MHz AOD drive frequency conditions corresponding to two different beam scan positions in the instrument, that generate the 120 MHz and 130 MHz heterodyne detected signals, respectively.

FIG. 4. Oscilloscope traces of the amplified outputs from the photoreceivers when our test material, i.e., a NLC cell is inserted in the scan beam in our instrument. (a) corresponds to the 60 MHz scan position, where the NLC cell is set to introduce a 180° optical phase shift to the scan beam, while (b) corresponds to the 65 MHz scan position, where the NLC cell is set to introduce a 90° optical phase shift to the scan beam.

phase over the wide AOD drive frequency band (in this case, 40 MHz) required for optical beam scanning of the test material—a result also expected from theory due to the common optical (and rf) path lengths.

Next, a test medium is inserted in the scan beam path— the reference signal and the test scan signal are no longer in-phase—which indicates the different optical path length caused by the different optical refractive index of the test material compared to the free-space/air medium through which the reference beams travel. Figure 4 shows the oscilloscope traces of the amplified outputs from the photoreceivers when our test material, i.e., a 6 μm thick parallel-rub birefringent mode NLC cell is carefully inserted into the scan beam in our instrument. The NLC cell is placed with its nematic director along the linear p polarization of the scanning optical beam. By changing the voltage level of the 1 kHz NLC cell drive signal, we can introduce any desired

optical phase shift between 0 and 3π radians, based on the given extraordinary refractive index of our NLC material, the active NLC material thickness, the cell glass wall thickness, and the glass wall refractive index. Thus, we use this large area (1 cm by 1 cm) NLC cell to simulate an optical phase plate with varying refractive indices. To simulate test material optical scanning, we record the heterodyne detected signal-pair traces for two different frequencies of Bragg cell operation, namely, 60 and 65 MHz, corresponding to different scan points along the x-direction on the NLC cell. In the first case [see Fig. 4(a)] corresponding to the 60 MHz scan position, the NLC cell voltage is set to introduce a 180° optical phase shift to the scan beam. This 180° optical phase difference relative to the reference beam is clearly shown by the equivalent 180° rf phase difference obtained between the heterodyne detected 120 MHz reference and scan signal sig-

nals. Because we are using a 532 nm laser wavelength, a 180° rf phase difference corresponds to a 266/n nm thick piece of transmissive material with a refractive index of n. To measure the test material optical thickness at a different position on the material along the x direction, we changed the AOD drive frequency to 65 MHz. In this second case [see Fig. 4(b)], the NLC cell voltage is set to introduce a 90° optical phase shift to the scan beam. Once again, this 90° optical phase difference relative to the reference beam is clearly shown by the equivalent 90° rf phase difference obtained between the heterodyne detected 130 MHz reference and scan signal signals. In this case, we simulated test material optical thickness of 133/n nm. Thus, using our instrument, we can rapidly measure optical material properties of a test medium, using the heterodyne detected rf phase shifted, high speed detector output signals.

An important issue related to the phase measurement accuracy of this instrument is the quality of the heterodyne detected signals that are used to make phase measurements via the electronic phase meter. Our experimental instrument was built on an optical table with no air isolation, and no special precautions were taken to reduce vibrations and air currents. Nevertheless, preliminary output signal carrier-to-noise ratio (C/N) measurements made using a rf spectrum analyzer indicate that high quality signals are generated by our instrument. In particular, direct power spectrum noise measurements are obtained using the rf power spectrum analyzer with an input filter resolution bandwidth (RBW) of 30 kHz. Figure 5(a) shows a measured C/N=108.9 dBc/Hz measured at a +160 kHz offset from the 120 MHz carrier. The output signal rf dynamic range was measured to be 59.3 dB [in Fig. 5(b)], with the noise floor level mainly controlled by the 40 dB gain power amplifier noise floor and the photoreceiver shot noise. Although no direct signal phase noise measurements were taken at present due to lack of custom instrumentation, we can indeed indirectly estimate this phase noise. It is well known from the radar community that accurate power spectrum measurements taken with a rf power spectrum analyzer can also give an indirect indication of the single sideband (SSB) signal phase noise.[22] This method is commonly known as the *direct spectrum* method, and converts the direct spectrum analyzer power reading to the SSB phase noise measurement $N_p(f_m)$, given in dBc/Hz at f_m offset by

$$N_p(f_m) = P_p(f_m) - P_c - 10 \log(B_{sa}) + P_{la}, \tag{5}$$

where $P_p(f_m)$ is the power level measured in dBm at the f_m offset frequency from the f_n carrier frequency, P_c is the power level measured in dBm at the f_n carrier, B_{sa} is the resolution bandwidth of the spectrum analyzer in Hz, and P_{la} is the +2.5 dB error correction for the characteristics of the spectrum analyzer's logarithmic amplifier.[22] Using our experimentally measured results where $f_n=120$ MHz and $f_m=160$ kHz (shown in Fig. 5), we get $P_p(f_m) - P_c = -59.3$, $B_{sa}=30\,000$. Thus, we can estimate the SSB phase noise in the heterodyne detected rf output signals from our experimental instrument to be -101.57 dBc/Hz at 160 kHz offset. Recall that we measured ~60 dB rf dynamic range or equivalent 30 dB optical dynamic range for our instrument.
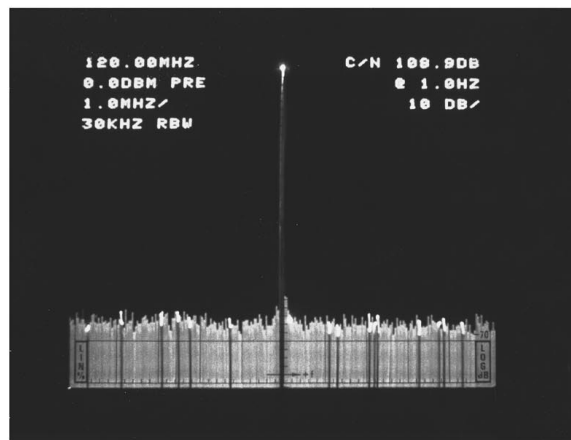
(a)
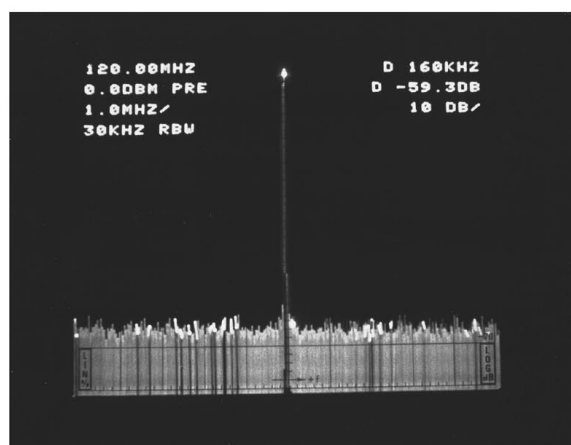
(b)

FIG. 5. (a) A measured C/N=108.9 dBc/Hz at a +160 kHz offset from the 120 MHz heterodyne detected signal from the instrument; (b) shows the measured output signal rf dynamic range to be 59.3 dB.

This indirectly implies that a 1/1000 of a fringe cycle can be measured using our instrument. These and other important system issues will be discussed later in the article.

B. Reflective mode design: Theory

In some application scenarios, it is beneficial to use a reflective geometry phase measurement setup. One example is when instrument size and weight must be minimized, or when the test medium itself is naturally reflective in nature, such as in mirror surface characterization. Since the transmissive-mode system in Fig. 2 is symmetric around the focal plane of lens S1, it can be reduced in volume by the use of a mirror at the focal plane, thus forming the reflective-mode scanning heterodyne optical interferometer shown in Fig. 6. Here, the mirror actually folds the system and retraces the light beams through AOD1 for the second Bragg diffraction; thus on the reflected path, AOD1 in Fig. 6 acts as the AOD2 in the transmissive case. Note that appropriate polarization optics must be used in this design to direct the input

a) TOP VIEW:

$2f_n$

Spatial Block

High Speed Photodetector Pair

F2

(+1, +1) & DC

S2

Sweep Generator

f_n

S1

Fixed Reference Beam

QWP or Faraday rotator (45° power)

Calibration Phase Cell

Mirror

C1

S

DC

p

s

p

s

s

p

CW Laser

PBS

AOD1 Bragg Cell

+1

Scanned Test Beam

n

Fixed Test Medium

Spatial Filter

F1

F1

s: horizontal polarization
p: vertical polarization (out of paper)
QWP: Quarter Wave Plate

b) 3-D VIEW:

Photodetector with phase Information

Mechanically scan point detector in y or use detector array and electronic scanning

Spatial Block

Fixed Reference Photodetector

y

x

Calibration Phase Cell

F2

S2

f_n

Fixed Reference Beam

Mirror

Spatial Filter

Objective Lens

C1

PBS

AOD1 Bragg Cell

S1

Electronically Scanned Test Beam

QWP or Faraday rotator (45° power)

Fixed Test Medium
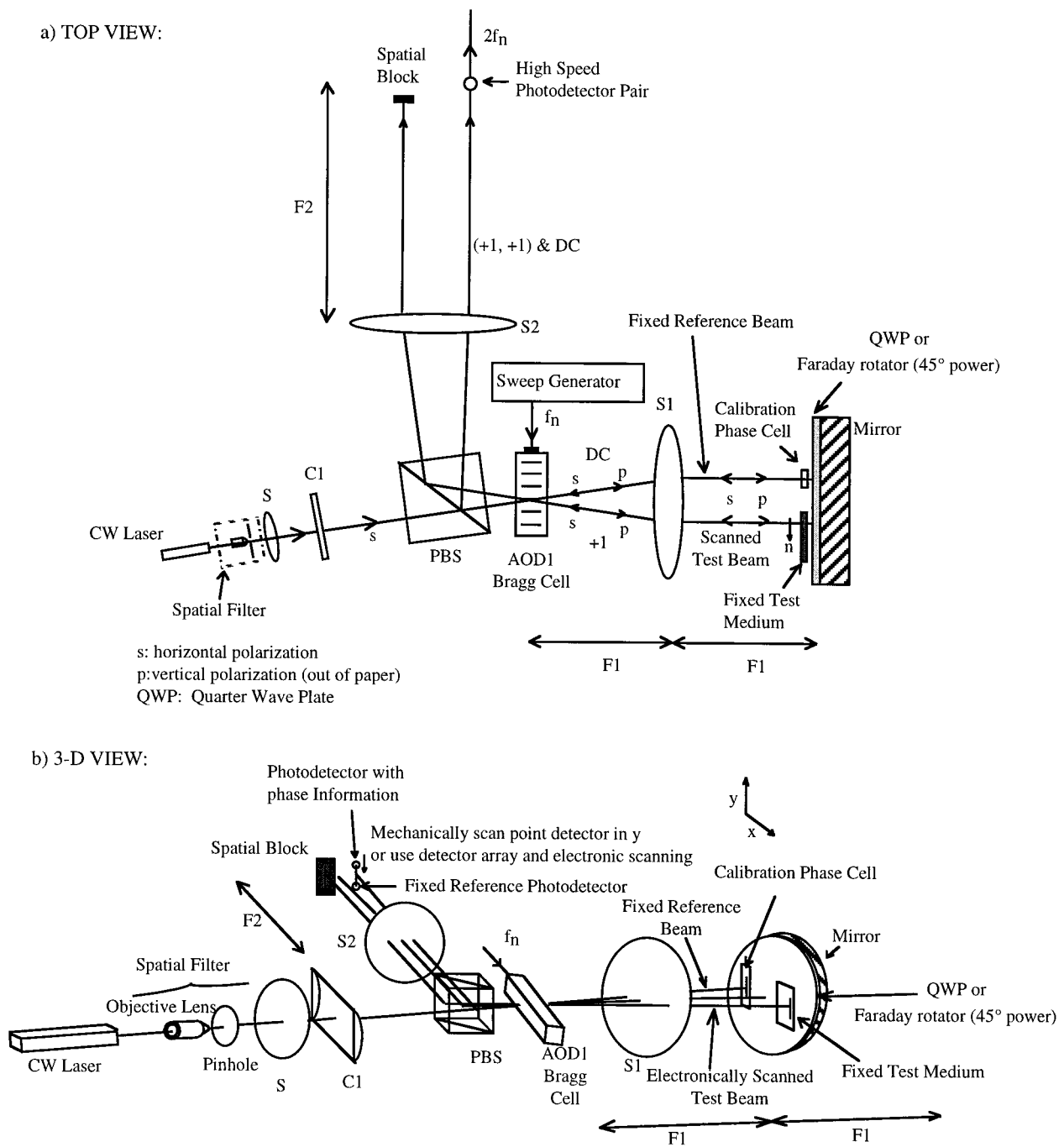
CW Laser

Pinhole

S

F1

F1

FIG. 6. The novel scanning heterodyne optical interferometer for reflective optical measurement and sensing applications. Both (a) top view and (b) 3D views are shown for this compact assembly instrument.

p-polarized laser light into the optical system and test medium, and to deflect the reflected s-polarized light coming from the test medium towards the photodetectors for heterodyne detection. A quarter wave plate (QWP) with its axis at 45° with the incident p-polarization ensures that the light returning back through AOD1 to the PBS is s-polarized and is therefore deflected by 90° by the PBS. Note the AOD must operate effectively for both p- and s-polarized light. With current thin film fabrication technology, it is possible to have a QWP deposited on a mirror surface, thus minimizing the number of independent optical components as each additional component is an additional phase noise source. A 45°

rotation power Faraday rotator can also be used instead of the QWP to give the instrument more robustness to component alignment accuracy and wavelength sensitivity. As in the transmissive interferometer, the reflective interferometer operates on the same +1 order double Bragg diffraction principles of Bragg cells, in this case, the single Bragg cell AOD1. Figure 6 also shows a simple three-dimensional view of our proposed novel scanning optical interferometer where one can see the physically separate high speed photodetectors that are critical for scan signal and reference signal generation via heterodyne detection.

IV. SYSTEM ISSUES AND FUTURE WORK

In this section, important system issues related to our proposed interferometers are considered. One issue is the accuracy of the optical phase measurement that depends on several optical and electronic component signal processing characteristics plus the instrument optical and electrical assembly. First, both the reference and scan signals generated by the photodetectors will have very similar phase noise characteristics because of the almost common-path optical architecture of the instrument. This can prove very helpful in reducing the phase noise in the processed phase-detector output signal as the phase-meter via electronic mixing of the scan and reference signals implements an electronic phase noise cancellation circuit. Other issues that control phase measurement accuracy are the standard electronic noise properties of the phase measuring optoelectronics and electronics such as photodiodes, amplifiers, rf cables, power supplies, and low pass filter which have been previously dealt with in detail in Ref. 6.

Mechanical and vibrational stability deserves attention because it is linked to output signal phase noise and, thus, phase measurement accuracy. In our instruments, because of the small number of optical components (e.g., four) that make the basic in-line interferometer, plus the almost common-path in-line design where both signal and reference optical beams travel in close proximity between the Bragg cells (in the transmissive design) or Bragg cell and mirror (in the reflective design), these beams suffer similar phase perturbations that are cancelled out on heterodyne detection at the photoreceiver. In other words, the phase noise in the interfering beams at the output plane is correlated, and the coherent heterodyne detection process at the photodetector cancels this noise. This gives our instrument a robust mechanical and optical design that has high resistance to vibrations and other environmental effects. Furthermore, because of the almost common-path optical design, a high coherence length, narrow spectral linewidth (e.g., 10 kHz) laser is not required, and the heterodyne detected output rf signal spectral linewidths are not altered by the laser linewidth. Thus, high cw or peak power lasers, which typically have broad (>10 MHz) spectral line widths, can be used with our instrument. Furthermore, because of the bulk-optics nature of the optical components used in the instrument, a higher optical power damage threshold is possible, implying use of very high power (e.g., cw 10 W) lasers for applications where high optical power is necessary, such as, combustion, shock wave, and turbulence experiments.

Another instrument design issue that controls the output rf signal noise characteristics is the quality of the Bragg cell drive rf signals. A Bragg cell drive signal with poor amplitude and phase noise values will propagate this noise through the optical instrument, and will result in a similarly poor amplitude and phase noise output rf signal from the photodetectors. Thus, a high quality rf sweep generator with low noise figure power amplifiers must be used to drive the Bragg cells. For our experiment, the power amplifiers had specified 10 dB typical noise figures (NFs), while the Wavetek model 5135A signal synthesizer had −125 dBc/Hz at +100 kHz and −135 dBc/Hz at +100 kHz specified am-plitude and phase noise values, respectively. From our experimental instrument, we measured −108.9 and −101.57 dBc/Hz amplitude and phase noise values, respectively, at +160 kHz offsets. Note that our measured instrument noise numbers −108.9 (amplitude) and −101.57 dBc/Hz (phase) and are very similar to the original rf signal noise numbers numbers of −115 (amplitude) and −105 dBc/Hz (phase) available from the instrument external signal processing electronics, after we have considered the 20 dB noise addition via the two 10 dB NF power amplifiers in the signal processing chain (i.e., amplifier at AOD drive input and amplifier after photodetection). Thus, within photodetection shot noise limits, high quality Bragg cell rf drive signals will generate high C/N rf output signals from the instrument, leading to improvements in instrument phase measurement accuracy.

Another system issue is the overall instrument optical efficiency, as this controls the type of laser required for a particular application. Optical power efficiency of our instrument η_s is approximately given by

$$\eta_s = [\eta_1 \eta_2 + (1-\eta_1)(1-\eta_2)], \tag{6}$$

where η_1 and η_2 are the first order Bragg diffraction efficiencies for AOD1 and AOD2, respectively. In our experiment, we measured $\eta_1 = \eta_2 = 0.4$ (or 40%), giving an overall instrument efficiency of 0.52% or 52%. Because we used a 100 mW cw laser, and a 10 times reduction neutral density filter at the output plane, we should have a total of ~5.2 mW of optical power for high speed photodetection. In our case, because all the components had no antireflection (AR) coatings, a slightly lower optical power was measured. Thus, depending on the application, a low power (e.g., 10 mW) laser can also be used in our instrument. As discussed briefly in Sec. III A, the modulation depth of the output rf signals from the photodetectors is related to the Bragg diffraction efficiencies and hence the optical powers P_{dc} and P_{scan} of the reference (dc) and scan signal ($+1 X+1$) optical beams, respectively. This modulation depth of the heterodyne detected output rf signals can be approximately expressed as

$$m_d = 2\sqrt{P_{dc}P_{scan}}/(P_{dc}+P_{scan})$$
$$= \frac{2\sqrt{(1-\eta_1)(1-\eta_2)\eta_1\eta_2}}{(1-\eta_1)(1-\eta_2)+\eta_1\eta_2}. \tag{7}$$

Recall that in our experiment, we measured $\eta_1 = \eta_2 = 0.4$ (or 40%). In this case, using Eq (7), we should expect the desired output modulation depth of $m_d = 0.923$. The experimental value was approximately $m_d = 0.9$. The ideal modulation depth for high efficiency heterodyne detection is $m_d = 1.0$, and occurs when $\eta_1 = \eta_2 = 0.5$ (or 50%).

Note that unlike Bragg cell based rf linear signal processing applications where Bragg cells need to be operated at low diffraction efficiencies of <10% to maintain linear rf-to-optical modulation of the input rf signals to generate high spurious-free two-tone dynamic range output signals—our instrument does not require low diffraction efficiency linear-mode Bragg cell operation. Because only single tone pure sinusoidal signals are fed to the Bragg cells at any given time in the instrument, no nonlinear intermodulation product

terms within the operational Bragg cell bandwidth (or device passband) are produced via the nonlinear high diffraction efficiency Bragg cell operation.[23] Thus, our instrument allows high diffraction efficiency (e.g., $\eta_1 = \eta_2 = 0.5$) Bragg cell operation that results in a maximum $\eta_s = 0.5$ or 50% over all optical power efficiency for the system.

There are several types of commercial Bragg cells that can be used with our instrument. The key differences in the devices are in the rf frequency of operation, AO interaction material, piezoelectric transducer size, and the time bandwidth product (i.e., device bandwidth X device time aperture) or storage capacity of the device. Most commercial AODs are either rf band (i.e., <100 MHz center frequency) devices, or microwave band (i.e., <2 GHz center frequency) wideband devices. For example, tellurium dioxide and flint glass are typical materials used in rf-band devices, while gallium phosphide (GaP) and lithium niobate are typical materials used in microwave-band devices.[24] Typically, Bragg cells have time bandwidth products that range from a 400 to 1000 cycles, implying that a high quality AO beam deflector can deflect an input laser beam through a maximum of 1000 scan points. For our instrument application, this means that the instrument can rapidly scan a 1000 independent points along the x direction on the test material. The point scan rate R depends on the AOD time aperture T, and is approximately given by $R = 1/T$, where in this case, the frequency of the AOD drive is changed every T seconds, with the frequency step rate being $1/T$. These are ideal scan conditions, and various scan system tradeoffs will have to be made based on laser beam illumination profiles, optical component apertures, switching speed of AOD drive signal generation electronics, and lens focal lengths.

The active distance the laser beam scans along the x direction using AOD1 is approximately given by

$$D_x = \{\theta_{\text{stop}} - \theta_{\text{start}}\} \text{F1}, \tag{8}$$

where

$$\theta_{\text{stop}}(\text{mrad}) = [\lambda(\mu m) \times f_{\text{stop}}(\text{MHz})]/[v_a(\text{mm}/\mu s)]$$

and

$$\theta_{\text{start}}(\text{mrad}) = [\lambda(\mu m) \times f_{\text{start}}(\text{MHz})]/[v_a(\text{mm}/\mu s)]. \tag{9}$$

Here the *start* and *stop* subscripts correspond to the optical scan start and stop positions (and AOD drive frequencies), respectively. In our experiment using flint glass AODs with a 40 MHz bandwidth centered at 70 MHz, F1=15 cm, and using $f_{\text{start}} = 50$ MHz and $f_{\text{stop}} = 90$ MHz, a total scan length of $D_a = 830$ μm along the x-direction is achieved with our instrument.

The Rayleigh resolution optical spot size diameter at the scan plane is approximately given by

$$\delta x(\mu m) = [2.44\lambda(\mu m)\text{F1}(\text{mm})]/[D_a(\text{mm})], \tag{10}$$

where D_a is the active optical beam diameter at the entrance of lens S1. In our case, $D_a \sim 1$ cm, thus giving us a beam spot size (along the x-direction) at the scan plane of ~ 19.5 μm. In our experiment, recall that we have a vertical optical line scanning along the x-direction. Based on these design numbers, our experimental instrument can scan a total of

$D_a/\delta x \sim 42$ spots along the test material. Improvements in both number of scan points and the area scanned can be made by careful design of the beam focusing optics, and by choosing the optimum AOD. For instance, if we used a GaP AOD—such as the one available from Brimrose Corp., Baltimore, MD—that has a $v_a = 6.3$ mm/μs and a bandwidth of 1 GHz, using the same optical setup (i.e., same F1 and λ), we can now scan a much larger length of $D_a = 12.67$ mm. Thus, depending on the instrument design, both small (<100 μm $\times$100 μm) or moderately large (e.g., 1.5 cm$\times$1.5 cm) regions of a test medium can be scanned using our systems.

The test medium phase map reconstruction method used with our instrument is similar to the two fiber sampling point scan method described for earlier heterodyne holography systems.[6] Previously, the two fiber scan method for interferogram reconstruction involved two fiber local sampling of the image plane, where one fiber at the interference plane can be stationary, i.e., the reference point, while the other fiber mechanically scans the moving fringe pattern on the interference plane to generate the phase data. The useful information for phase map reconstruction obtained by this method includes the number of fringes crossed during the scan process and the interpolation value of the phase within one fringe. In our instrument, in essence, we implement the same data collection and reconstruction process, where here, instead of mechanically moving detectors, we have an electronically scanned optical beam to simulate the motion of the moving fiber/detector. Like the two fiber scan method, we still have a fixed detector that provides the reference phase information for later interpolation. In our case, by electronically scanning the read laser beam over the test medium, we have also simulated a moving fringe pattern at the output interference plane where we have placed our two sampling detectors.

In conclusion, we have proposed two novel scanning heterodyne optical interferometers. One design is transmissive in nature while the other design is reflective. Other variations of this basic design are also possible, including high speed 2D optical scanning systems.[20] To show basic instrument working principles, the transmissive instrument is experimentally demonstrated in the laboratory using flint glass rf Bragg cells and a NLC test medium for introducing spatially varying phase perturbations. Heterodyne detected signals having frequencies from 100 to 180 MHz are generated based on the test material beam scan position. Output signal C/N and SSB phase noise are measured and estimated, respectively, providing preliminary phase measurement sensitivities of 1/1000 of a fringe cycle. Important instrument system issues such as beam scan speed, test beam scan area, optical system power efficiency, laser source spectral linewidth, and AOD rf drive signal quality, have been discussed. Other issues such as photodetector rf output signal phase noise, scan beam spot size, number of scan points, instrument mechanical and vibrational stability, instrument calibration, and phase map reconstruction have also been discussed. Future work relates to demonstration of the reflective design scanning heterodyne optical interferometer and further optimization of the overall optical and electrical designs for the instruments. Furthermore, these instruments will be tested for a variety of interferometric measurement applica-

tions, and accurate phase measurements using high performance phase meters will be implemented and discussed to determine ultimate instrument performance limits. Extensions to 2D and 3D point scanning interferometric instruments and their various applications will also be studied.[25]

ACKNOWLEDGMENT

[1] P. Hariharan, *Handbook of Optics*, 2nd ed. edited by M. Bass (McGraw-Hill, New York, 1995), Vol. II, Chap. 21, p. 21.1.

[2] *Springer Series in Optical Sciences* edited by P. K. Rastogi (Springer, New York, 1994), Vol. 68.

[3] J. Schwider, *Progress in Optics* (North Holland, Amsterdam, 1980), Vol. 28, p. 273.

[4] K. Creath, in Ref. 2, p. 5.

[5] J. H. Bruning, D. R. Herriot, J. E. Gallagher, D. P. Rosenfeld, A. D. White, and D. J. Brangaccio, Appl. Opt. **13**, 2693 (1974).

[6] R. Dändliker, in Ref. 3, Vol. 17, p. 1.

[7] J. Mastner and V. Masek, Rev. Sci. Instrum. **51**, 926 (1980).

[8] R. Dändliker and B. Eliasson, Exp. Mech. **19**, 93 (1979).

[9] R. Thalmann and R. Dändliker, Appl. Opt. **26**, 1964 (1987).

[10] E. Gelmini, U. Minoni, and F. Docchio, Rev. Sci. Instrum. **66**, 4073 (1995).

[11] N. A. Riza, Ph.D. thesis, California Institute of Technology, 1989.

[12] N. A. Riza, IEEE Photon. Technol. Lett. **4**, 177 (1992).

[13] N. A. Riza, IEEE Photon. Technol. Lett. **4**, 1073 (1992).

[14] N. A. Riza, IEEE/OSA J. Lightwave Technol. **10**, 1974 (1992).

[15] N. A. Riza, Appl. Opt. **33**, 3712 (1994).

[16] N. A. Riza, Appl. Opt. **33**, 3060 (1994).

[17] N. A. Riza, IEEE Photon. Technol. Lett. **7**, 339 (1995).

[18] N. A. Riza, Proc. SPIE **2155**, 413 (1994).

[19] N. A. Riza, Appl. Opt. **31**, 3194 (1992).

[20] N. A. Riza, *OSA Topical Meeting on Holography* (OSA, Washington, DC, 1996).

[21] N. A. Riza and M. C. DeJule, Opt. Lett. **19**, 1013 (1994).

[22] S. J. Goldman, *Phase Noise Analysis in Radar Systems* (Wiley, New York, 1989), p. 91.

[23] D. R. Pape, IEEE Ultrasonics Symposium Proceeding, 1989, p. 509.

[24] N. Uchida and N. Niizeki, Proc. IEEE **61**, 1073 (1973).

[25] N. A. Riza (Patent filed).